Dynamometer Power Output Measurements of Piezoelectric Actuators

E. Steltz and R.S. Fearing
Department of EECS, University of California, Berkeley, CA 94720
{*ees132 ronf*} *@eecs.berkeley.edu*

***Abstract*— Piezoelectric bending actuators are an attractive option for driving microrobots due to their light weight, scalability, ease of integration and high bandwidth. However, the only existing energy or power output measurements for piezoelectric bending actuators have been extrapolated from DC values or unloaded AC values and are most likely overestimates. For microrobot applications such as flapping flight, accurate measures of power density are critical. In this work, to properly measure the energy output of a 10mg piezoelectric actuator, a custom dynamometer is designed and constructed to directly measure the power output at various frequencies and conditions. The dynamometer can simulate a pure resistive load at resonant frequencies from 1 to 100Hz. Due to low internal damping and fracture limits, actuators cannot be run in the matched condition at high fields ($>$ 1 V/μm). Using the device, energy output per cycle at 1.6 V/μm was measured to be a maximum of 19.1 μJ/cycle (232 μm amplitude, 30Hz), giving a delivered energy density per cycle of 1.89J/kg. Internal actuator damping was measured at 1 V/μm to account for an energy loss of only 0.21μJ per cycle (232 μm amplitude, 30Hz).**

I. Introduction

Piezoelectric bending actuators have been utilized in many areas of robotics, such as to flap the wings of a micro air vehicle [1], to actuate control surfaces for indoor slow fliers [2], and even for motors for legged microrobots [3],[4]. However, in dynamic robots where piezoelectric actuators are the main source of actuation, the power output of these actuators is still unknown.

Several researchers have addressed some issues regarding power output and power density for piezoelectric actuators. In the field of piezoelectric transformers, efficiency limitations are discussed in [5]. Pomirleanu [6] has reported power outputs for piezoelectric stack actuators, but only for quasi static conditions (which in our experience is likely an overestimate). Near [7] has extrapolated constituent equations to predict power output for popular bimorph and other piezoelectric actuators (such as RAINBOW). In [8], energy densities for the same 10mm bimorphs that we are testing in this work are predicted from DC measurements.

It is widely known that the properties of piezoelectric actuators (such as d_{31} and the Young's modulus) can change drastically when the actuators are subject to high fields or high displacements [9] [10]. In addition, extrapolating behaviors as simple as maximum strain in the piezoceramic (such as the large strain values found in [11]) are invalid since these values are only internally induced strain; external mechanical strain can make the piezoceramic fail prematurely, especially when it is simultaneously actuated via an electric field. The effect of nonlinearities such as creep, hysteresis, saturation, etc. can obviously reduce power output of piezoelectric actuators, but to the authors' knowledge this has not been quantified at sufficient field (only up to 0.1V/μm in [10]).

This work was supported by NSF IIS-0412541

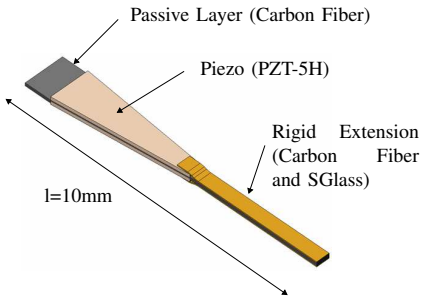

Fig. 1. 10mg piezoelectric bending actuator

This work focuses on measuring the power output of the 10mm piezoelectric bending actuators discussed in [8], used to drive the wings of a 100 mg flapping wing air vehicle [1]. These 10mg actuators are composed of PZT-5H actuation layers with a carbon fiber elastic layer and glass fiber/carbon fiber extension as shown in Fig. 1. In order to measure the power output and delivered power density for these actuators, a custom dynamometer was designed to actively measure force and displacement of an actuator and therefore compute power output. The dynamometer contains another actuator that can actively simulate varying loads (varying stiffness, mass, and damping). Our goal is to run our device under test (DUT) at frequencies up to 100Hz and explore the actuator's behavior as frequency, displacement, and voltage drive level are varied.

II. Dynamometer Design

To control the applied force on the DUT running at 100Hz, we need another (larger) actuator with a bandwidth above the desired operating frequency. In order for piezoelectric actuators to run in a reasonably efficient way, we must run the DUT as if it was driving a load at resonance [12]. In order to do so, the Driver actuator in the dynamometer must simulate various stiffnesses and masses, in addition to acting as a desired damping value. This allows us to choose the resonant frequency and oscillation amplitude of the simulated load below the overall system resonant frequency.

The driver actuator (another, larger piezoelectric bimorph) is attached to the DUT via a lightweight spring with a known

spring constant. Custom optical position sensors accurate to about 1 μm are used to monitor the position of both actuators [13]. The setup appears in Fig. 2.

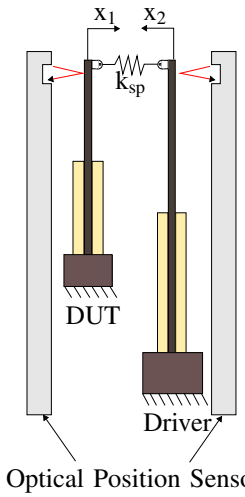

Fig. 2. Schematic of proposed dynamometer

A. Dynamic Model of Piezoelectric Bending Actuator

A piezoelectric bending actuator can simply be modeled as a force source (representing the piezoelectric plate) in parallel with a spring (representing the elastic layer) [14]. At high frequencies, we must also include the damping losses (coming from a variety of sources such as the matrix in the composite layers, hysteresis, and other piezoelectric nonlinearities) and mass of the actuator. In this case, the mass term is an equivalent mass derived from the distributed mass of the actual actuator.

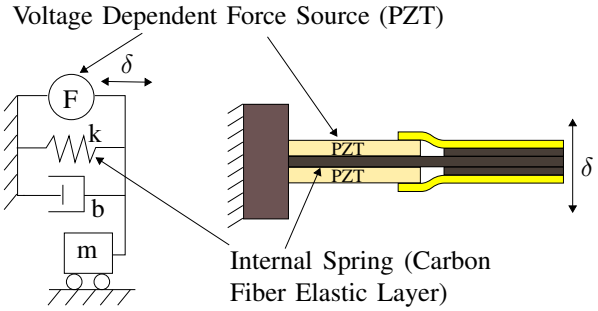

Fig. 3. Second order model of a cantilever bending actuator

This simple second order model is far from an exact model for the actuator in that it does not contain any direct expressions for creep, hysteresis or saturation. However, if we look at the frequency response of the actuator subject to an input of 10V amplitude and the frequency response of a model fit with appropriate stiffness, mass, and damping (via least squares, see Table II-A), one can see that the second order model is a fair approximation of our bending actuator (Fig. 4). The resonant peak of the actuator is significantly wider than the model's and slightly asymmetric; this can be

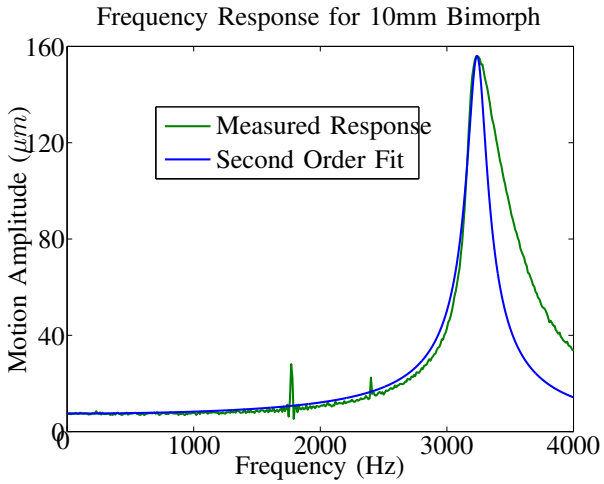

Fig. 4. Frequency response (magnitude Bode plot) for 10mm bimorph (10V amplitude drive or 0.08V/μm)

TABLE I
SECOND ORDER BEST FIT MODEL PARAMETERS

Parameter	Fit Value
k	$250N/m$
b	$5.9 * 10^{-4}Ns/m$
m	$6.0 * 10^{-7}kg$

explained by softening in the actuator at high displacements, which of course the model does not account for. Up to the resonant peak, however, a second order model is more than sufficient to properly predict the frequency response of the actuator.

B. Dynamic Model of Entire Dynamometer

If we use our simple model for a single piezoelectric bending actuator in Fig. 3 and apply it to our proposed dynamometer in Fig. 2, we have the complete model in Fig. 5. Here we have included mass and damping in the connecting spring (functioning as our force sensor) for completeness.

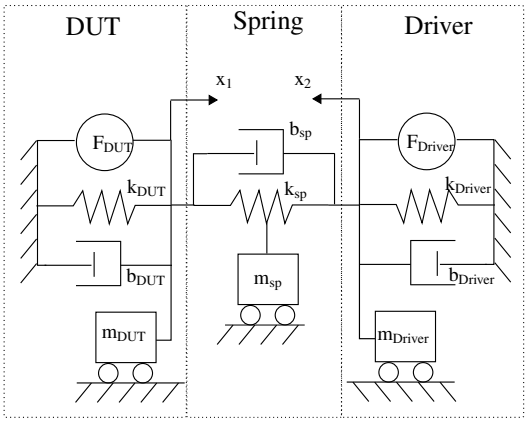

Fig. 5. Block diagram of dynamometer

The work output of the DUT in the setup of Fig. 5 can be expressed as

$$W = \int_{x_0}^{x_f} F dx_1 \tag{1}$$

where F is the force output of the DUT. If we express this in terms of velocity and time (for oscillatory inputs), we have

$$W = \int_{t_0}^{t_f} F v_1 dt \tag{2}$$

where W here is energy output per oscillation cycle. If we represent the actuator positions x_1 and x_2 as the sum of their sinusoidal harmonics

$$x_1 = \sum_{n=1}^{\infty} A_n \sin(\omega n t + \phi_n) \tag{3}$$

$$x_2 = \sum_{n=1}^{\infty} B_n \sin(\omega n t + \psi_n) \tag{4}$$

$$v_1 = \dot{x_1} = \sum_{n=1}^{\infty} A_n n\omega \cos(\omega n t + \phi_n) \tag{5}$$

and we express the force output of the DUT as, in general,

$$F = k_{sp}(x_1 + x_2) + b_{sp}(\dot{x_1} + \dot{x_2}) + m_{sp}(\ddot{x_1} + \ddot{x_2}) \tag{6}$$

and substitute our expressions for positions, velocities, and forces into (2), we have the energy output of the DUT in terms of the energy in the spring mass, damping, and stiffness:

$$W_k = A_n B_n \pi k_{sp} \sin(\phi_n - \psi_n) \tag{7}$$

$$W_b = A_n \pi \omega b_{sp}(A_n + B_n \cos(\phi_n - \psi_n)) \tag{8}$$

$$W_m = A_n B_n \pi m_{sp} \omega^2 \sin(\phi_n - \psi_n) \tag{9}$$

where W_k is the energy delivered to the spring element, W_b is the energy delivered to the damping element in the connecting spring, and W_m is the energy delivered to the mass of the spring.

The total energy output per cycle (W_n) and total power output P of the DUT can then be written as

$$W_n = W_k + W_b + W_m \tag{10}$$

$$P = \sum_{n=1}^{\infty} \frac{W_n n\omega}{2\pi} \tag{11}$$

If m_{sp} and b_{sp} are significant, to properly measure power output we must include W_b and W_m from (8) and (9). However, at low frequencies, these two terms are very small and we won't need the values for m_{sp} and b_{sp} which are difficult to extract. It is also important to remain at high enough frequency that creep effects are negligible. We have noticed creep in these actuators up to around 10Hz; we will include a factor of safety here and assume that at 30 Hz creep effects are negligible but we are still at low enough frequency that W_b and W_m are negligible compared with W_k. Note that the driver damping, inertia, and spring properties do not enter in the energy delivery calculations.

III. Dynamometer Construction

Constructing the driver actuator is quite straightforward; it is virtually the same process as for our small DUT except the size is scaled up. The connecting spring is a challenging design problem, however. First, the spring should have low mass and damping so that we can neglect the effect of its mass (m_{sp} in (9)) and damping (b_{sp} in (8)). The spring also needs to be linear. We also need it to be removable from the DUT and driver actuator so that the DUT can be changed. Finally, the spring must connect to both actuators in such a way that their bending does not cause any type of binding in the system. In theory, this is simply achieved by putting pin joints at the attachment points of the two actuators (as is shown in Fig. 2), but in practice at this scale pin joints have hysteresis and friction and also weigh too much.

The solution to the spring design problem is shown in Fig. 6, with the actual constructed spring shown in Fig. 7. Our spring is made of carbon fiber bent around a mold during curing, then glued to two separate, smaller arcs cured in the same manner. The main span is the linear spring element; the two arcs at the end of the spring relieve the moment due to bending of the two actuators by employing Kevlar fiber, strung tightly between the arcs. The Kevlar fiber is very compliant to moments since it is made up of several threads that are wound together. Since the actuators are not perfectly parallel, the string also serves to allow small off-axis deflections. Stiff carbon fiber planks were glued permanently onto the Kevlar string to attach the planar ends of the actuators with a low melting point plastic.

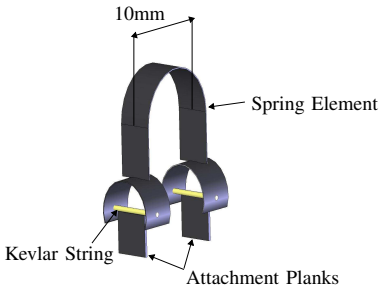

Fig. 6. Schematic of custom dynamometer spring

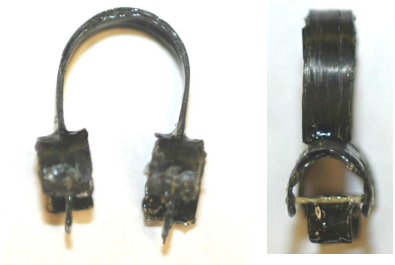

Fig. 7. Front and side view of carbon fiber dynamometer spring

The entire dynamometer with both actuators, connecting spring, and position sensors is shown in Fig. 8. Horizontal

and vertical micropositioning stages were employed to line up the spring prior to attachment. To calculate the spring constant of our connecting spring, which can vary slightly for different attachments, we run each DUT once connected and measure the Driver deflection. Since we always use the same Driver, we measured its stiffness a priori at a known drive voltage corresponding to the dynamometer neutral position (k_{Driver} = 475 N/m at 125V). If our DUT tip displaces x_1 and our driver (which is passive for this test) displaces x_2 and has stiffness k_{driver}, the stiffness of the connecting spring k_{sp} is

$$k_{sp} = \frac{k_{driver} x_2}{x_1 - x_2} \tag{12}$$

Noticing that we have a subtraction of two rather small displacements in the denominator of this expression and a possibly small displacement in the numerator, we matched the stiffness of the connecting spring to our driver actuator so that the expression in (12) does not vary widely with small displacement errors (typical k_{sp} = 400 N/m).

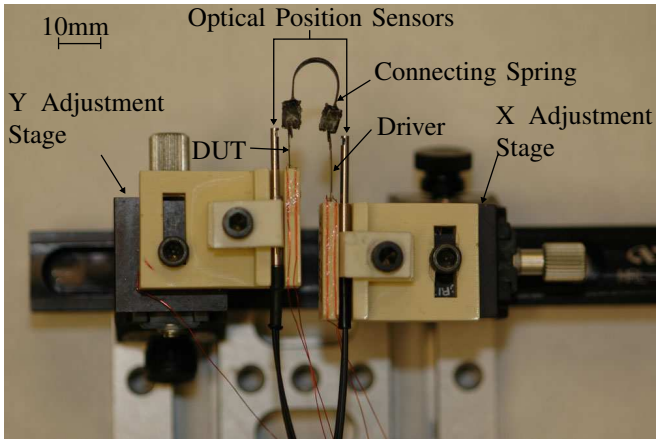

Fig. 8. Picture of dynamometer test setup

IV. Dynamometer Verification

A. Bandwidth Verification

We tested the bandwidth of the entire system when the DUT and Driver are simultaneously connected through k_{sp}. As can be seen from Fig. 9, the resonant frequency of the system is approximately 320Hz, which satisfies our requirement of being over 100 Hz. However, the system has a very high mechanical Q; this means that it will be very easy to excite the main resonant mode when driving at lower frequencies. Thus to avoid resonances from 2nd and 3rd harmonics of the drive, we use drive signals $<$ 100Hz. Note that the positions x1 and x2 are 180 degrees out of phase at DC; this is due to the positive directions of the two displacements shown in Figure 2 being in opposite directions.

B. Verification of Maximum Power at Resonance

At resonance, the spring and mass of a dynamic system produce and absorb no net energy per cycle. Under this

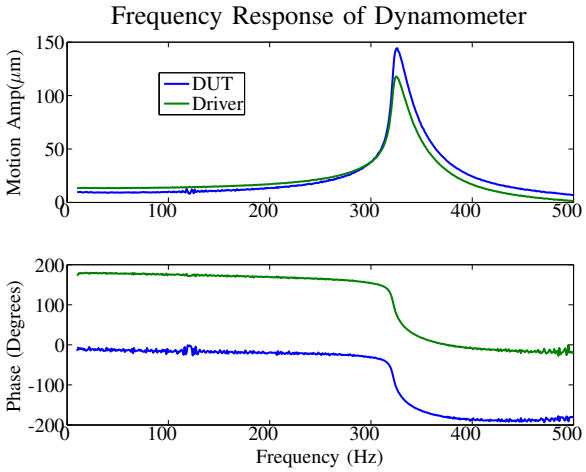

Fig. 9. Bode plot driving the Driver actuator of the dynamometer. DUT plot is for position x1 of Fig 2 and Driver plot is for position x2 of Fig 2.

condition, the actuator only performs work on its internal damping and the damping of the load. Therefore, if we calculate the energy output per cycle of the DUT from (7) (we only include the spring term for now because m_{sp} and b_{sp} are negligible at 30 Hz), we should see a peak when the input voltage to the DUT is 90 degrees out of phase with the position of the DUT. As seen in Fig. 10, indeed the power output of the DUT is maximum at 90 degrees within an allowable phase error (about 1 degree).

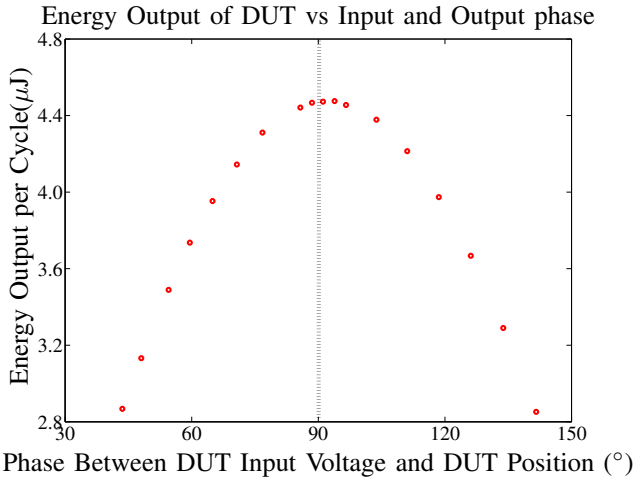

Fig. 10. Verification of maximum power at resonance (90 degrees), 1 V/μm

C. Sample Work Loop

A work loop was plotted in Fig. 11 to further verify the system's behavior. The standard work loop curve is observed (see [15], [16] or [17] for more on actuator or muscle work loops). The useful work which we will report later in this paper (for this trial 5.9 μJ per cycle) is the area inside the work loop of Fig. 11. The shape of the work loop is not perfectly symmetric due to expected hysteresis.

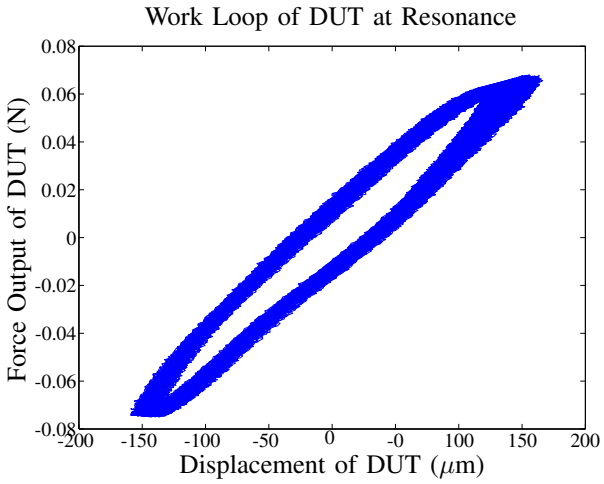

Fig. 11. Work loop of DUT at 125V drive, 150 μm amplitude of displacement

V. Power Output Measurements

From [8], we expect our 10mm, 10mg actuators to fracture at an average motion amplitude of 190 μm. To make sure each actuator survives all the tests, we include a factor of safety here and only run the DUTs up to 150 μm of amplitude. The measured power output at simulated resonance (30Hz) for a typical 10mm actuator is shown in Fig. 12.

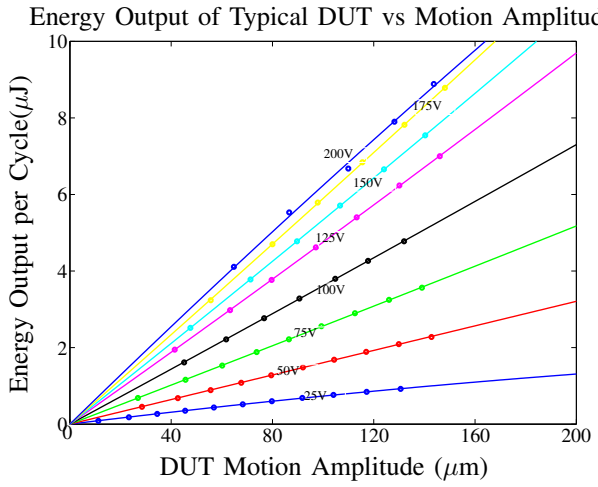

Fig. 12. Typical power output curves for 10mg bimorph

Several interesting observations can be made from Fig. 12. First, one can see that the power output is saturating as we drive the DUT at very high ($> 125V$) voltages. Even though the power output is still modestly increasing, we do not expect to see much additional power output above 200V amplitude drive (1.6 V/μm) and did not test above this amplitude.

Using a simple linear system analysis, we fit the data in Fig. 12 to our linear model. At resonance, the internal force source of the actuator only does work on its own internal damping and the simulated damping introduced by the driver (i.e. no net work on the mass and spring elements). If we denote the internal actuator damping as b_{act} and the simulated load damping b_{load}, then the useful work output of the DUT is given by

$$W = b_{load} A_1^2 \omega^2 \int_0^T \cos^2(\omega t + \phi_1) = b_{load} A_1^2 \omega \pi \quad (13)$$

At our resonance condition,

$$F = (b_{act} + b_{load}) v_1 \quad (14)$$

Using another assumption of a linear system, the force source of the DUT in Fig. 5 is sinusoidal and only depends on the voltage on the actuator, or

$$F = F(V) \cos(\omega t + \phi_1) \quad (15)$$

Combining with (14) and (13), the work output of the actuator for a given voltage drive is

$$W = [\pi F(V)] A - [\pi b_{act}] A^2 \omega \quad (16)$$

We fit this model via least squares to the data in Fig. 12. The curves appearing in Fig. 12 are work output parabolas, reaching a maximum when the load damping matches the internal actuator damping. However, the peak of these parabolas would only be observed if the actuator could withstand much more than 150 μm of motion; we are only observing the very front edge of each parabola. Since in all these drive amplitudes the parabola would peak for only much greater amplitudes, we cannot accurately fit the curvature (the squared amplitude term of (16)) since the linear term in (16) is dominating. Even though we expect the internal damping of the actuator to vary with drive voltage, we cannot accurately extract b_{act} from this analysis method.

We measured energy output for 5 actuators. As can be seen from Fig. 13, some deviation is observed likely due to hand assembly. The linear part of (16) was fit to the actuator data via least squares. The error from each data point to the least squares fit mean was calculated and divided by the least squares fit value to find a percentage error vector. The standard deviation of this percentage error vector is given in Table II.

TABLE II
Error characteristics for least squares fit to data in Fig. 13

Drive Amplitude Fit	Std. Dev. of % Error	Energy/Volt (μJ/V)
50V	7.2	0.048
100V	8.3	0.052
150V	6.2	0.053
200V	7.7	0.047

A. Extrapolation to Higher Frequencies

All results presented thus far were run at 30 Hz to avoid limitations discussed in Section IV. To find the behavior of the actuator at higher frequencies and to verify that we do not need to include the spring mass and damper energy

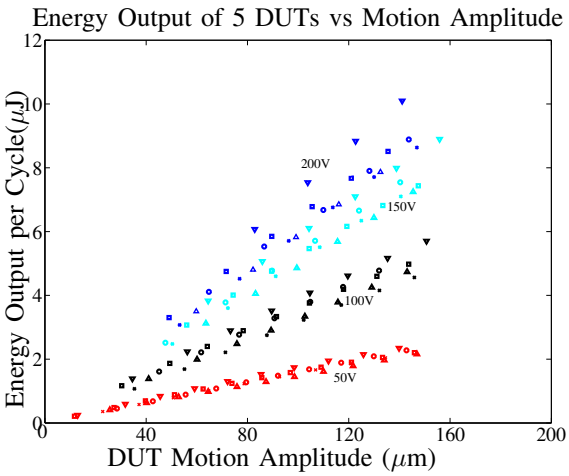

Fig. 13. Power output for 5 different 10mm bimorphs

terms ((9) and (8)), the DUT was driven at a constant voltage amplitude and kept at a constant displacement (in this case, 125V amplitude drive, 100 μm amplitude displacement). The drive frequency was varied between 20 and 100Hz in vacuum and air (to eliminate the possibility of air damping). Energy output of the DUT was taken at resonance for each frequency as seen in Fig. 14.

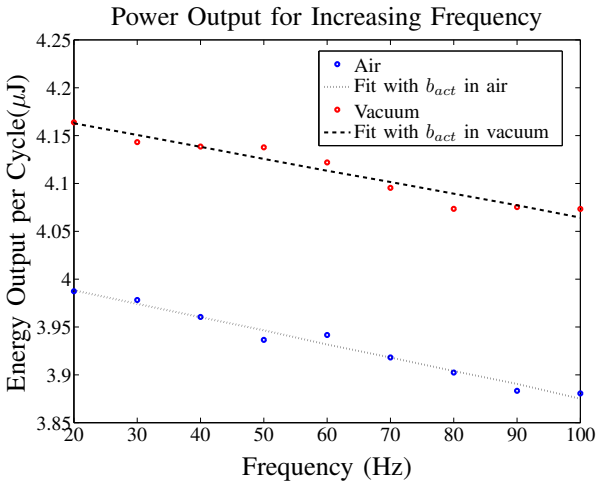

Fig. 14. Behavior of dynamometer with increasing frequency

In Fig 14 we are again measuring the work done per cycle on the load damping, given by (13). In other words we are just counting the work done on the load damping, not the work done by the DUT on its own internal damping. However, since we are keeping the displacement and voltage drive constant, for all frequencies we would expect that the work output per cycle is a constant equal to the total work done by the internal force source of the DUT, or

$$W_{Total} = W_{b_{load}} + W_{b_{act}} = C \tag{17}$$

We can then extract the damping in the DUT actuator, b_{act}, through a least squares fit of the slope of the data in Fig. 14, which is also plotted. We find when we average the two slopes of the lines, at 125V drive, $b_{act} = 0.0066 Ns/m$. This value corresponds only to a 3% loss in energy output from 20Hz compared with 100Hz for our 100 μm amplitude, 125V trial. The authors would like to note that again the mass and damping of the spring were neglected, so strictly speaking this value of b_{act} is an upper bound, but the mass of the spring is very small and its damping is most likely negligible simply through its construction.

VI. Improvements to Actuator Performance

Recent findings in [18] has suggested that a special cutting technique could reduce the size of edge cracks along our bimorph actuators which govern their fracture. The technique involves only scoring the PZT-5H using laser micromachining, then cleaving the edge on the score line. When the actuators were assembled, the cleaved edge (most likely containing fewer or smaller microcracks) faced outward on the actuator, where the maximum strain occurs. In principle, this could improve the amplitude at which the actuators fracture and therefore increase their power density through higher displacement.

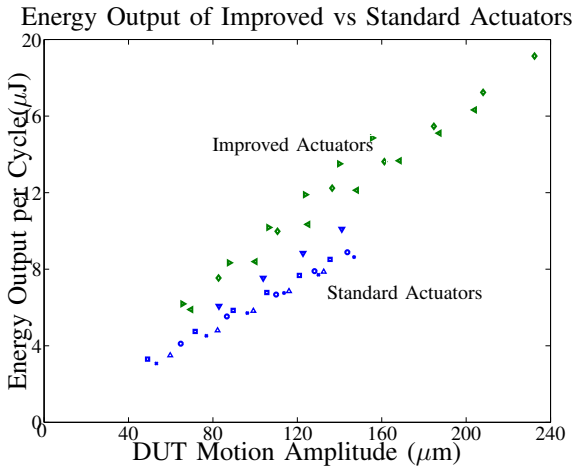

Fig. 15. Comparison of improved actuator and standard actuator performance. Both were driven at 200V amplitude.

As seen from Fig. 15, the performance of the actuators improved significantly, and not just by increasing the available displacement before fracture. In fact, the power output of the actuator was significantly better at all amplitudes. The authors hypothesize that since the actuators are very small (1.5mm wide at the base), edge crack effects are probably very significant. Thus we can improve our performance tremendously by reducing edge cracks through the mentioned cleaving process. Fig. 15 includes results from three of our improved actuators, but the driver actuator, even when increased in size from previous tests, could not test these actuators to fracture. Therefore, the maximum energy output per cycle shown in Fig. 15 of 19.1 μJ/cycle is only a lower bound until the actuators can be tested all the way to fracture. The standard actuators were easily fractured if tested beyond 150 μm.

VII. Conclusion and Future Work

We have achieved several milestones in measuring the power output of miniature piezoelectric bending actuators. To our knowledge, we have made the first active measurement of force and displacement of piezo bending actuators up to 100Hz. In addition, our dynamometer has the capability of simulating any reasonable real or imaginary load on the DUT. We used this capability to simulate actuators driving a load at resonance.

Regarding the power output of our piezoelectric actuators, we have shown that the internal damping of the actuator is not a significant source of loss. We have also shown that for maximum power output, the actuators should be run at very high voltage amplitudes (200V or 1.6 V/μm). Our maximum energy output results are summarized in Table III. The reader is encouraged to note that the predicted value for energy density in Table III is itself extrapolated from DC predictions and does not include losses in the material; therefore it is most likely not attainable since the actuator is oscillating.

TABLE III

Energy output characteristics for 10mg piezoelectric bimorph actuators

Parameter	Predicted in [8]	Standard	Improved
Mass (mg)	11.72	10.1	10.1
Energy Output (μJ/cycle)	27.5	9.5	$>$19.1
Energy Density (J/kg)	2.35	0.94	$>$1.89
b_{act} @ 1V/μm (Ns/m)	0.0052 [14]	0.0066	–

We have shown that the actuators cannot be run with a matched load damping for maximum power transfer; this would require that the actuators go through high displacements that have been shown to cause fracture. However, increasing the actuator amplitude before fracture, done by reducing edge microcracking, directly leads to higher energy outputs. When this was done through a new manufacturing process which involved cleaving the PZT-5H, both energy output at lower amplitudes and increased amplitude at fracture were indeed observed. However, the actuators were not tested all the way to fracture, so the energy output shown (19.1 μJ/cycle) is only a lower bound.

Finally, we compare our actuator to the flight muscle of an actual flying insect (a typical Dipteran) with the estimates of Table IV (data from [19]). The improved piezoelectric bending actuator, operating at 275 Hz (a typical flapping frequency of our micromechanical flying insect prototype) at 200V drive would produce 4.7mW of useful work output (including a 0.53mW or 11% loss from the internal damping of the actuator). This yields a power density of 476W/kg, easily beating the estimate for Dipteran muscle power density in Table IV. This also compares favorably to other available millimeter scale actuators such as the rotary piezoelectric motor of [20] with a power density of 81W/kg.

VIII. Acknowledgments

The authors thank Prof. Robert Wood for numerous discussions regarding actuator improvement.

TABLE IV

Estimate of Dipteran insect power generation

Typical Power Density	% Muscle Mass	Implied Muscle Power Density
70 W/kg	35	200W/kg

References

[1] R. J. Wood, S. Avadhanula, M. Menon., and R. S. Fearing, "Microrobotics using composite materials: The micromechanical flying insect thorax," in *IEEE International Conference on Robotics and Automation*, Taiwan, 2003, pp. 1842–1849.

[2] R. J. Wood, S. Avadhanula, E. Steltz, M. Seeman, J. Entwistle, A. Bachrach, G. Barrows, S. Sanders, and R. S. Fearing, "Design, fabrication and initial results of a 2g autonomous glider," in *The 31st Annual Conference of the IEEE Industrial Electronics Society*, 2005.

[3] R. Sahai, E. Steltz, S. Avadhanula, R. Wood, and R. Fearing, "Towards a 3g crawling robot through the integration of microrobot technologies," in *IEEE Int. Conf. on Robotics and Automation*, 2006.

[4] M. Goldfarb, M. Gogola, G. Fischer, and E. Garcia, "Development of a piezoelectrically-actuated mesoscale robot quadraped," *Journal of Micromechatronics*, vol. 1, pp. 205–219, 2002.

[5] A. Flynn and S. Sanders, "Fundamental limits on energy transfer and circuit considerations for piezoelectric transformers," *IEEE Transactions on Power Electronics*, vol. 17, pp. 8–14, 2002.

[6] R. Pomirleanu and V. Giurgiutiu, "High-field characterization of piezoelectric and magnetostrictive actuators," *J. of Intelligent Matl. Sys. and Struct.*, vol. 15, pp. 161–180, 2004.

[7] C. Near, "Piezoelectric actuator technology," in *Proc. of the Smart Struct. and Mat. Conf*, vol. 2717, 1996.

[8] R. J. Wood and E. Steltz, "Optimal energy density piezoelectric bending actuators," *Sensors and Actuators A*, vol. 119/2, pp. 476–488, 2004.

[9] K. Uchino, J. Zheng, A. Joshi, Y. Chen, and S. Yoshikawa, "High power characterization of piezoelectric materials," *J. of Electroceramics*, vol. 2, pp. 33–40, 1998.

[10] Q. Wang, Q. Zhang, B. Xu, R. Liu, and L. Cross, "Nonlinear piezoelectric behavior of ceramic bending mode actuators under strong electric fields," *J. Appl. Physics*, vol. 86, pp. 3352–3360, 1999.

[11] S. Park and T. Shrout, "Ultrahigh strain and piezoelectric behavior in relaxor based ferroelectric single crystals," *J. Appl. Phys.*, vol. 82, pp. 1804–1811, 1997.

[12] E. Steltz, M. Seeman, S. Avadhanula, and R. S. Fearing, "Power electronics design choice for piezoelectric microrobots," in *IEEE/RSJ Int. Conf. on Intelligent Robots and Systems*, 2006.

[13] E. Steltz, R. J. Wood, S. Avadhanula, and R. S. Fearing, "Characterization of the micromechanical flying insect by optical sensing," in *IEEE Int. Conf. on Robotics and Automation*, 2005.

[14] R. J. Wood and E. S. and, "Nonlinear performance limits for high energy density piezoelectric bending actuators," in *IEEE Int. Conf. on Robotics and Automation*, 2005.

[15] M. Dickinson, C. Farley, R. Full, M. Koehl, R. Kram, and S. Lehman, "How animals move: An integrative view," *Science*, vol. 288, pp. 100–106, 2000.

[16] A. Ahn, K. Meijer, and R. Full, "In situ muscle power differs without varying in vitro mechanical properties in two insect leg muscles innervated by the same motor neuron," *J. Exp. Biol.*, vol. 209, pp. 3370–3382.

[17] K. Meijer, M. Rosenthal, and R. Full, "Muscle-like actuators? a comparison between three electroactive polymers," in *Smart Structure and Materials 2001: Electroactive Polymer Actuators and Devices. Proc. SPIE*, Y. Bar-Cohen, Ed., vol. 4329, 2001, pp. 7–15.

[18] R. J. Wood, "Design, fabrication, and analysis of a 3dof, 3cm flapping wing mav," in *IEEE Int. Conf. on Intelligent Robots and Systems*, 2007.

[19] R. Dudley, *The Biomechanics of Insect Flight*. Princeton University Press, 2000.

[20] J. Palmer, J. Mulling, B. Dessent, E. Grant, J. Eischen, A. Gruverman, A. Kingon, and P. Franzo, "The design, fabrication, and characterization of millimeter scale motors for miniature direct drive robots," in *IEEE Int. Conf. on Robotics and Automation*, 2004.